



A synthesis of graphene quantum dots/hollow TiO₂ nanosphere composites for enhancing visible light photocatalytic activity

Hongjuan Zhang¹ · Zunli Mo¹ · Hebing Pei¹ · Qianqian Jia¹ · Ruijuan Wang¹ · Hangkong Feng¹ · Ruibin Guo¹ · Nijuan Liu¹

Received: 25 September 2019 / Accepted: 26 November 2019 / Published online: 16 December 2019
© Springer Science+Business Media, LLC, part of Springer Nature 2019

Abstract

Given the versatility and value of the semiconductor composites for photocatalysis, we reported a new, friendly environment, high specific surface area material of the graphene quantum dots/hollow titanium dioxide nanosphere (GQDs/H-TiO₂) composites which are synthesized through a simple hydrothermal method. GQDs (~ 5 nm) exhibit highly photoluminescent and widely visible light absorption properties. H-TiO₂ has high surface area and abundant exposed active sites for photocatalysis. The research demonstrates that GQDs coupled on H-TiO₂ can effectively enlarge the light absorption of the H-TiO₂ to visible region (~ 650 nm) and enhance the electron–hole pair separation efficiency of GQDs/H-TiO₂ composites owing to GQDs acting as an electron repository and electron transport bridge. In our delight, the photocurrent enhancement of newly prepared GQDs-3.0/H-TiO₂ composite electrode was almost 3.5 times higher in comparison with that in pure H-TiO₂ electrode at an applied voltage of 0.5 V using Na₂SO₄ (0.5 M) solution as the electrolyte. In addition, the photocatalytic activity of the prepared GQDs-3.0/H-TiO₂ (96.9%) on the degradation of Rhodamine B (RhB) was also significantly enhanced compared with that of pure H-TiO₂ (33.3%) after 180 min. The protocol is suitable not only for the GQDs-modified semiconductors photocatalysts but also provides further insights to apply GQDs to other energy conversion devices.

1 Introduction

Graphene quantum dots (GQDs) are common existing in numerous 0-dimensional nanomaterials of the graphene families which are widely used in electronics [1–3], energy conversion/storage devices [4, 5], sensors [6, 7], biomedicine [8, 9], and photocatalysis [10, 11]. Given the ubiquitous electronic properties of the GQDs, for instances outstanding optical properties [12], low toxicity [13], excellent catalytic performance [14, 15], and semiconducting properties [16, 17], the various GQDs have been reported in the recently

years. Generally, the electronic properties of the GQDs are largely dependent on the band gap and the electron–hole pairs which were produced through absorbing photon [18]. In particular, the band gap of GQDs can be controlled by sizes or functionalization, and thus the variety of fluorescence can be obtained under UV illumination (red, blue, and green, etc.) [19–21]. However, GQDs have a weak visible light absorption which significantly limits its practical application. It was found that heteroatom (N, B, and S)-doped GQDs with broad absorption band and excellent luminescence stability, they were also act as a critical role in sensitizing and improving the catalytic properties of the semiconductors [22, 23].

Photocatalytic reaction driven by sunlight has a rich history in address the increasingly serious environmental and energy issues and how to develop and optimize high produce efficiently photocatalytics for degradation under visible light have attracted much research interest [24]. Among these reported photocatalysts approaches, TiO₂ has been demonstrated as a widely used semiconductor material due to its low toxicity, availability, and outstanding physical and chemical stability [25]. Despite their excellent performances and stabilities, the slightly

Electronic supplementary material The online version of this article (<https://doi.org/10.1007/s10854-019-02657-3>) contains supplementary material, which is available to authorized users.

✉ Zunli Mo
mozlnwnu2010@163.com

¹ Research Center of Gansu Military and Civilian Integration Advanced Structural Materials, Key Laboratory of Eco-Environment-Related Polymer Materials, Ministry of Education of China, College of Chemistry and Chemical Engineering, Northwest Normal University, Lanzhou 730070, China

narrow band gap value of anatase TiO_2 (3.2 eV) determines that it can only use 3–5% of ultraviolet radiation from sunlight, limiting its widely application under natural light. In order to obtain TiO_2 with high photocatalytic activity, various intrinsic and extrinsic approaches have been reported, including preparing nanostructure semiconductors [26, 27], introducing heteroatoms [28], coupling with different semiconductors or dyes [29, 30], and controlling morphology [31]. In generally, the employing of chalcogenide materials (CdS, PdS, CdS, etc.) with narrow band gap can obtain sensitizing semiconductor materials, but these semiconductors exhibit a rapid photocorrosion and certain environmental problems during the experiment [32, 33]. In addition, carbon nanomaterials have a rich history in material science and have become a promising approach for enhancing the photocatalytic transformations owing to their superior conductivity, great chemical stability, low toxicity, and outstanding optical properties. The variety of carbon nanomaterials include (multi-walled) carbon nanotubes [34], graphene [35], partially reduced graphene oxide [36], and graphene (oxide) quantum dots [37, 38]. Among these carbon nanomaterials, significant developments have been made on the photocatalysis of GQDs in recent years. Though GQDs have been revealed unique advantages toward photoinduced electron transfer, the pure GQDs catalytic activity is limited due to the large exciton binding energy. Usually, we can use GQDs acting as effective electron sensitizer or cocatalyst and combining with semiconductor TiO_2 nanoparticles to enhance photocatalytic ability. GQDs can improve the photoelectric properties of GQDs/ TiO_2 composites, and we developed photoelectrochemical characterizing approaches to study the mechanism of photoelectric performance of GQDs/ TiO_2 .

We demonstrate a new versatile and environmentally friendly one-step hydrothermal route to synthesize GQDs/hollow TiO_2 nanosphere (GQDs/H- TiO_2) composites. Particularly, the achieved H- TiO_2 with uniform size (250 nm), large specific surface area (223.48 m^2/g), and high exposed active sites, and quantum-sized GQDs with oxygen-containing functional groups and abundant defect edges were uniformly distributed and incorporated on the surface of porous H- TiO_2 nanospheres; these potential active sites of GQDs and H- TiO_2 for photocatalytic reaction together suggest that GQDs/H- TiO_2 has enhanced photocatalytic activity. The degradation of Rhodamine B (RhB) of GQDs/H- TiO_2 composites with different weight contents of GQDs was investigated, and the maximum removal rate of GQDs-3.0/H- TiO_2 reaches 96.9% after 180-min irradiation. Meanwhile, photoelectrochemical characterizations further demonstrate that the addition of GQDs significantly improved the electrochemical activity of GQDs/H- TiO_2 . To the best of our knowledge, this is the first report to research the photoelectric

properties of GQDs decorated on H- TiO_2 , which would extend the photocatalytic application of GQDs/H- TiO_2 composites.

2 Experimental section

2.1 Materials and characterizations

Flame-retardant expandable graphite (expansion capacity 250 cm^3/g) was purchased from Qingdao Nanye Hongda Graphite Products Co., Ltd. Concentrated sulfuric acid, phosphoric acid, and nitrogen were obtained from Yantai Shuangshuang Chemical Co., Ltd. *N,N*-dimethylformamide (DMF) was bought from Wuhan Chujiang Haoyu Chemical Technology Development Co., Ltd. Hydrogen peroxide (H_2O_2) was purchased from Baiyin Chemical Reagent Factory. Glacial acetic acid, potassium permanganate, and tetrabutyl titanate (TBOT, 98%) were purchased from Sinopharm Chemical Reagent Co., Ltd. (Shanghai, China). Formaldehyde and melamine were obtained from Shanghai Zhongtai Chemical Reagent Co., Ltd. Hexadecyltrimethyl ammonium bromide (CTAB) was purchased from Shanghai Lianshuo Biotechnology Co., Ltd. RhB was purchased from Shanghai Jingchun Reagent Co., Ltd. All conventional chemicals were of analytical grade and were used without further purification.

SEM was obtained using the JSM-6701F scanning electron microscopy. TEM was characterized using JEM-2010 high-resolution field emission microscopy. Laser scattering particle size distribution was analyzed using a LA-960 (Horiba, Kyoto). XRD patterns were carried on a D/Max-2400 powder diffractometer with a monochromatic $\text{Cu K}\alpha$ X-ray radiation. UV–vis absorption spectra were determined using a UV–vis spectrophotometer (Shimadzu UV 2550). Photoluminescence (PL) was acquired from a fluorescence spectrometer (Fluoro Max-4, Horiba, Kyoto). FTIR was carried out on a EQUINOX55 spectrometer with KBr pellets (Thermo Fisher Scientific, Shanghai). The specific surface areas, microporous surface area, and pore size distribution were calculated based on the Brunauer–Emmett–Teller method, *t*-plot method, and the nonlocal density functional theory method. TG was investigated by operating Shimadzu DT-40 Instrument in N_2 atmosphere protection and a heating rate of 10 $^\circ\text{C}/\text{min}$. X-ray photoelectron spectroscopy (XPS) was measured by an Axis Ultra spectrometer with $\text{Al K}\alpha$ X-ray radiation.

2.2 Preparation of graphene quantum dots (GQDs)

GQDs were synthesized via a top-down process from three-dimensional graphene network materials (3DGNs) [39, 40]. The procedures were as follows: (1) preparation of expanded

graphite. The flame-retardant expandable graphite was transferred to a Midea microwave oven and expanded for 30 s to obtain expanded graphite. Expanded graphite was added in the DMF solution at a ratio of 1 mg/mL, and sonicated at 100 W until the expanded graphite was wetted and completely dispersed. Subsequently, the samples were rinsed with ultrapure water and ethanol three times to obtain clean expanded graphite. (2) Preparation of graphite oxide (GO). A modified Hummers' method was carried out for the synthesis of GO [41]; 1 g of expanded graphite, 120 mL of H_2SO_4 , and 15 mL of H_3PO_4 aqueous solution were mixed and stirred at 5 °C for 20 min. Afterward, 9 g of KMnO_4 was added slowly under continuous stirring at 5 °C. Then the mixture was stirred at 50 °C for 12 h. Mixture was slowly poured into a prepared 150 mL of ice water mixture under continuous stirring, and ice was added until the temperature of the solution system reached room temperature. After the reaction, the remaining permanganate and manganese dioxide can be reduced by H_2O_2 (2 mL, 30%), and the color of the suspension turned from brown to bright yellow. After that, GO was collected by centrifugation (8000–10,000 rpm) and washed with HCl (20 mL, 2%), ethanol, and ultrapure water for several times to achieve a suspension pH of 7. GO was dried in a vacuum freeze-drying at $-50\text{ }^\circ\text{C}$ for at least 12 h and stored for further applications. (3) Preparation of the 3DGNs. 3DGNs were prepared by one-step hydrothermal method with GO solution (1 mg/mL) as precursors, ammonia (v/v 5%), and hydrazine provide (v/v 2.5%) conditions for the reduction reaction. The mixture was treated in a Teflon-lined stainless autoclave at 180 °C for 12 h. The obtained 3DGNs were washed with ultrapure water and then freeze dried. (4) Preparation of GQDs. GQDs were prepared by chemical oxidation treatment of 3DGNs, and 0.01 g of 3DGNs was dissolved in 20 mL of concentrated nitric acid solution. The mixture was kept at 150 °C for 20 h under the condition of the condensing device. After that, the condensing unit was disassembled and the mixture was stirred until a brown GQDs sample appears in the reactor. For purification of GQDs, the solution of GQDs was dialyzed (retained molecular weight 8000 Da) for 24 h. Then GQDs dried in a vacuum freeze-drying at $-50\text{ }^\circ\text{C}$ at least 12 h and stored for further applications.

2.3 Synthesis of hollow TiO_2 nanospheres (H- TiO_2), GQDs/H- TiO_2 composites

TiO_2 was prepared by template method. Briefly, template melamine formaldehyde microsphere (MF) was prepared according to a report [42]. The formaldehyde (9.8 g) was added into 200 mL of water and heated to 80 °C, and subsequently melamine (2.5 g) was dissolved in the mixture. To adjust pH to 3.8, glacial acetic acid was added into the mixture. A white emulsion was obtained after stirring for

20 min, and the obtained MF microspheres were washed with ultrapure water for several times. Then 0.05 g CTAB, 1 mL $\text{NH}_3\cdot\text{H}_2\text{O}$, and 1 mL H_2O were dispersed into MF suspension (100 mL, 2%) and kept stirring for 20 min. After that, 15 mL of TBOT was added dropwise to the mixture and kept stirring for 4 h, and then the products were collected by centrifugation and washed thrice to collect sediments. Finally after vacuum freeze-drying at $-50\text{ }^\circ\text{C}$ for 12 h, we obtained core-shell microspheres consisting of MF as the cores and TiO_2 as the shells. H- TiO_2 was obtained by calcination at 500 °C for 2 h at a heating rate of 1 °C/min in a tube furnace under N_2 atmosphere. In addition, in order to optimize the hollow spherical structure of H- TiO_2 , the effects of $\text{NH}_3\cdot\text{H}_2\text{O}$, TBOT and reaction time were studied through the orthogonal experiments using $L_9(3^3)$. GQDs/H- TiO_2 composites were prepared by a simple hydrothermal method. The mixture of H- TiO_2 (0.1 g) and GQDs dispersions (20 mL) was processed by ultrasonication (70 W, 20 kHz) for 1 h, and then transferred to a Teflon-lined autoclave (50 mL) for further hydrothermal treatment at 100 °C for 3 h. Next, the mixture was centrifuged and the sediment was washed twice with ultrapure water. The amount of GQDs added in the solution was 1.5, 3.0, and 4.5 mg, respectively, resulting in composites that were denoted as GQDs-*x*/H- TiO_2 , where *x* refers to the mass ratio of the GQDs to GQDs/H- TiO_2 .

2.4 Photoelectrochemical measurements

The photoelectrochemical tests were conducted on an electrochemical workstation (CHI 660E, Shanghai Chenhua, China) by constructing a three-electrode system. A 300-W Xe lamp (HSX-F300, Beijing NBet) with a cutoff filter ($\lambda \geq 400\text{ nm}$, UVCUT400, Beijing NBet) was used for a simulated visible light source. The counter electrode was Pt wire, the reference electrode was a Ag/AgCl electrode, and the electrolyte solution was 0.5 M Na_2SO_4 solution. The working electrode was prepared as follows: 10 mg of the GQDs/H- TiO_2 composites was ultrasonically dispersed in the mixture of isopropanol (495 μL), ultrapure water (495 μL), and Nafion (10 μL , 5%, Du Pont Corp.) for 0.5 h. Subsequently, 100 μL of the obtained suspension was coated on a $1 \times 1\text{ cm}^2$ indium tin oxide (ITO) glass before drying at room temperature.

Photocatalytic activity of composites was evaluated through decolorization of RhB in a photochemical reaction quartz trap under visible light irradiation. The intensity value of light was determined to be 100 mW/cm² after evaluating by a light power meter (CEL-NP2000, Education Au-light, China). Before visible light irradiation, the mixture of GQDs/H- TiO_2 (25 mg) and RhB solution (50 mL, 10 mg/L) was stirred in the dark for 1 h. Then, the visible light is irradiated to start the photocatalytic reaction. A certain volume of supernatant is taken from the reaction quartz

trap at a specified time. The photocatalytic reaction was analyzed by recording the change of the maximum absorbance at 554 nm by the UV–vis spectrophotometer. The removal rate of RhB was defined as the equation $\eta\% = (1 - C/C_0)\%$ ($C/C_0 = A/A_0$), where C_0 represents initial concentration of RhB, C indicates the concentration of reactant, A_0 denotes the absorbance value of initial RhB, and A stands for the absorbance value of reactant.

3 Results and discussion

3.1 Morphology and structural characterization of samples

As illustrated in Scheme 1, TBOT was used as titanium source hydrolyzed in a mixed solvent [$v(\text{alcohol})/v(\text{water})$: 100:1] and subsequently MF microspheres were coated with TiO_2 . In order to create pores in the wall of the final hollow sphere, we use CTAB as the surfactant and ammonia acts as catalyst. H- TiO_2 spheres were obtained after selective removal of the organic MF core by calcinations in air. During the calcination process, shrinkage of the titanium shell could take place resulting in H- TiO_2 with size smaller than the MF core template. GQDs/H- TiO_2 could be synthesized by one-step hydrothermal process to ensure a better adherence of GQDs on the surfaces.

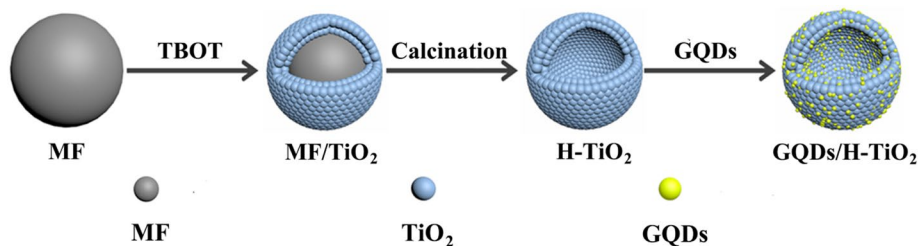
H- TiO_2 was prepared by a template method as illustrated in Scheme 1. Due to perfectly matched particle size and strong surface interaction between MF and TiO_2 , we choose MF and TiO_2 to prepare the core–shell MF/ TiO_2 composite. Initially, the uniformly sized MF nucleus was first synthesized through the resinification of melamine and formaldehyde. Figure 1A displays the SEM micrograph of the templating agent MF, from which we can see uniformly dispersed MF microspheres with diameter of approximately 2.1 μm , which were consistent with the results of the laser particle size analysis characterized in Fig. 1B (geometric mean diameter 2.1070 μm). We selected MF core to prepare the core–shell MF/ TiO_2 composite with a large diameter because of its better dispersity compared to TiO_2 with a diameter of 10 nm. The excellent dispersity is critical for uniformly coating with TiO_2 . In addition, MF microspheres with abundant nitrogen-containing groups ($-\text{OH}$, $-\text{NH}$,

$-\text{NH}_2$) are positively charged in the reaction system [43]. After introducing the titanium source, the slow hydrolysis process allows the nano- TiO_2 to effectively adhere to the surface of MF microspheres without further modification. Figure 1C, D includes the morphology and microstructure information of H- TiO_2 , which was formed with an average diameter about 250 nm; meanwhile, nano- TiO_2 particle roughly aggregates on the surface of shell. Increasing the quantity of the TBOT, the increased average diameter and rough surface of the shell were increased revealing that TiO_2 has been coated onto the surface of MF microspheres by the in situ hydrolysis, condensation, and coating process [42]. After calcination treatments, the TiO_2 outer shell was shrunk to obtain a shell with a dense and stable structure due to the removal of MF and the densification of the loose outer shell. Figure 1D also shows a broken nanosphere further confirms the hollow properties structure of H- TiO_2 .

To gain insight into the optimization of the experimental conditions and the determination of the process parameters, a series of orthogonal experiments was carried out. We consider the three critical factors including volume of $\text{NH}_3 \cdot \text{H}_2\text{O}$, TBOT mass fraction, and reaction time. Three levels were set for each factor and the $L_9 (3^3)$ orthogonal array was used to arrange the tests. The factors and levels of the orthogonal experiments are shown in Table S1. The experimental scheme designed according to the $L_9 (3^3)$ orthogonal table is shown in Table S2. According to Table S2 and the results of SEM images shown in Fig. S1, during the forming process of the shell TiO_2 coating layer, the order of the three main factors priorities is as follows: volume of $\text{NH}_3 \cdot \text{H}_2\text{O}$ > content of TBOT > reaction time. Thus, the best optimized process is volume of $\text{NH}_3 \cdot \text{H}_2\text{O}$ 1 mL, TBOT mass fraction 1%, and reaction time 4 h.

The surface functional groups of MF were detected using FTIR in Fig. 2A. Absorption bands at 813 cm^{-1} , 1006 cm^{-1} , 1165 cm^{-1} , 1557 cm^{-1} , and 3380 cm^{-1} are assigned to the bending vibrations of C–N–O, C–O–C, C–N, $-\text{NH}_2$, and $-\text{OH}$ bonds [44]. However, no MF-related peaks were found in the spectrum of H- TiO_2 , demonstrating that the MF structure was clearly removed after the calcination treatments. FTIR spectra of GQDs were collected and results are shown in Fig. 2B. The 3400 cm^{-1} , 2816 cm^{-1} , and 1730 cm^{-1} peaks were caused by the stretching vibrations from O–H, C–H, and C=O. Bands at 1615 cm^{-1} , 1383 cm^{-1} , and 1103 cm^{-1}

Scheme 1 Illustration of the formation of GQDs/H- TiO_2 composites



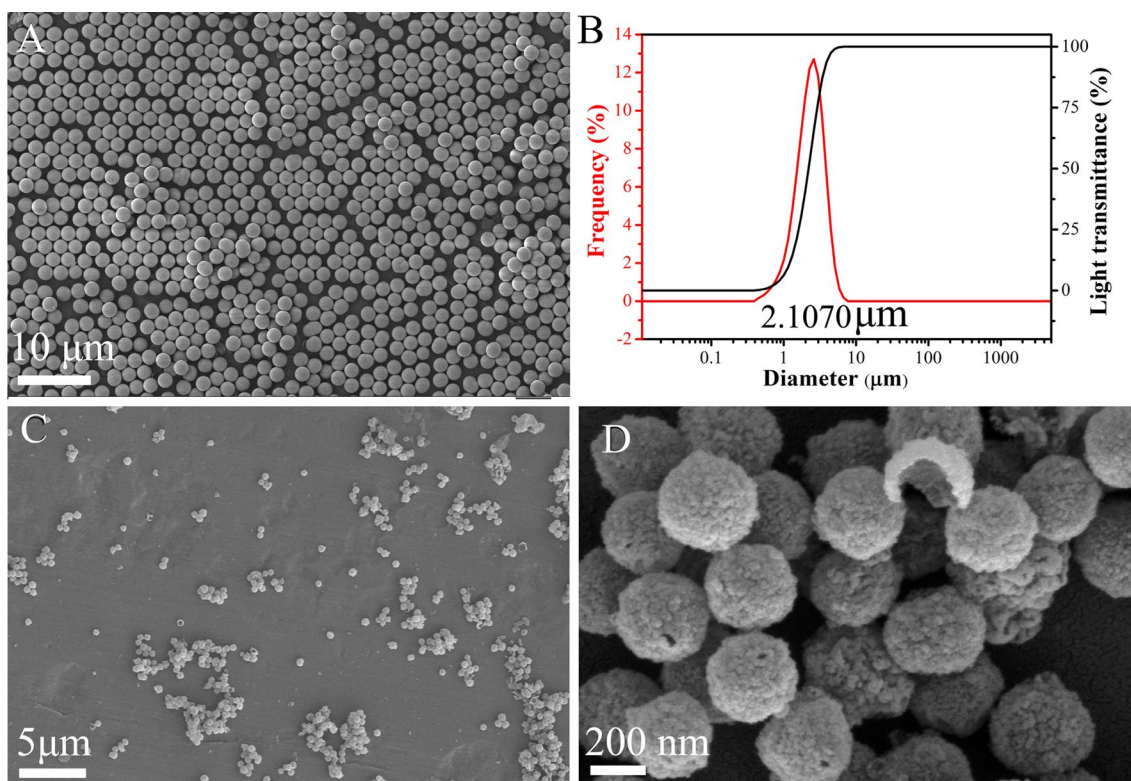


Fig. 1 **A** SEM image of MF microspheres. **B** Laser particle size analysis of MF microspheres. **C** and **D** SEM images of pure H-TiO₂ at different magnifications

come from the vibrations of C=C, C–N/N–H, and C–O–C bonds, respectively [45]. These functional groups derived from oxidative cutting of 3DGNs improve the hydrophilicity and stability of GQDs in aqueous systems [46, 47]. In the case of pure H-TiO₂, broad absorption bands at 400–800 cm⁻¹ correspond to Ti–O–Ti bands [48]. After decorating with GQDs, the oxygen-containing functional groups, including C=O, C–O–C, C=C, and –OH, were introduced to the surface of GQDs-3.0/H-TiO₂. Simultaneously, a significant red shift of the Ti–O bond was observed due to the addition of GQDs [38].

Because the FTIR characterizations only indicate the surface structure of products, then we further performed the TG analysis to confirm the effects of GQDs on the thermal stability of composites. As seen in Fig. 2C, for the pure H-TiO₂, a 3.1% weight loss was detected and two weight loss regions can be observed: the weight loss below 200 °C was ascribed to the evaporation of water, and the weight loss at higher temperature range explained the existence of GQDs and MF calcined residue. By contrast, GQDs-3.0/H-TiO₂ composite was thermally stable up to 900 °C and almost no mass loss in the whole process, indicating that the thermal stability of GQDs-3.0/H-TiO₂ was enhanced.

The XRD patterns of H-TiO₂ and GQDs/H-TiO₂ composites displayed in Fig. 2D. H-TiO₂ has obvious characteristic

diffraction peaks that agreed with the standard data of an anatase TiO₂ (JCPDS Card No. 21-1272) by the exposure of 25.2°, 37.7°, 47.9°, 53.8°, 55.0°, and 62.6° peaks, corresponding to the reflections from (101), (004), (200), (205), (211), and (204) crystal planes, respectively [49]. Compared with pure H-TiO₂, low amount and highly dispersed GQDs have no effect on the diffraction peak of GQDs/H-TiO₂ except for the decrease of peak intensity, and the results agreed with the reported references [50]. GQDs have relatively low diffraction intensity so that the diffraction peak intensity of composites decreased obviously (Fig. 2D1). N₂ adsorption/desorption analysis was carried out to estimate the porosities of H-TiO₂ and GQDs-3.0/H-TiO₂ composite. Isotherms are assigned to the typical type IV and shown obvious hysteresis loop at the relative higher pressure than 0.45, indicating the presence of mesopores (Fig. 2E). The average pore diameter according to BJH calculated from nitrogen isotherms is 2.5–7 nm (Fig. 2E1), which has an important contribution to the combination of the GQDs. However, the GQDs (~5 nm) are more likely to combine with mesopores; this result also was confirmed in the later TEM results. The uniform mesopores are formed by removing CTAB which can provide abundant exposed active sites for photochemical reactions and serve as a continuous electron highway, benefiting the construction of the

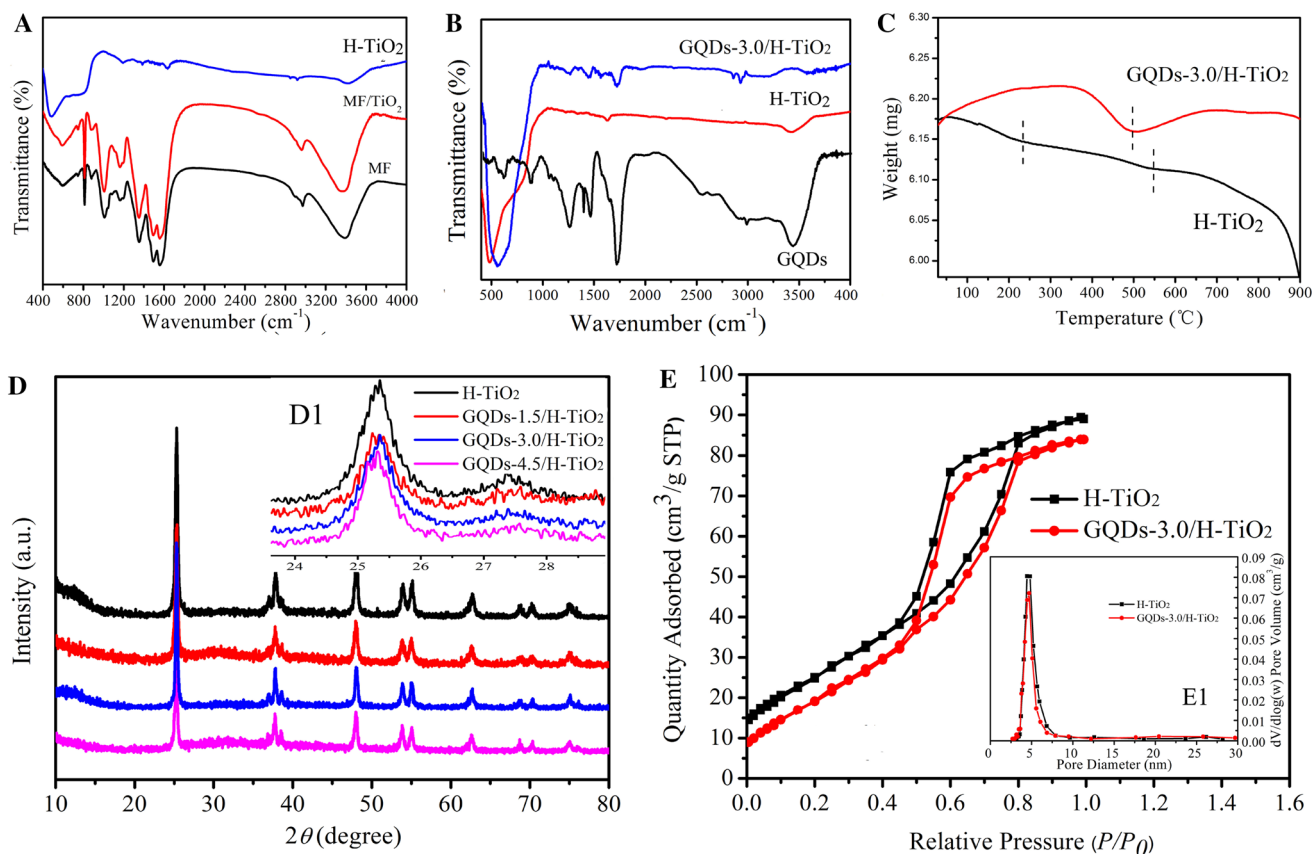


Fig. 2 **A** FTIR spectra of MF, MF/TiO₂, and H-TiO₂. **B** FTIR spectra of GQDs, H-TiO₂, and GQDs-3.0/H-TiO₂. **C** TG curves for the bare H-TiO₂ and GQDs-3.0/H-TiO₂. **D** XRD patterns of H-TiO₂, GQDs-1.5/H-TiO₂, GQDs-3.0/H-TiO₂, and GQDs-4.5/H-TiO₂. **D1** Partially

enlarged view of the XRD pattern. **E** N₂ adsorption/desorption isotherms of H-TiO₂ and GQDs-3.0/H-TiO₂. **E1** Pore size distributions of bare H-TiO₂ and GQDs-3.0/H-TiO₂

large electron-accessible surface area. The specific surface area slightly decreased from 223.48 m²/g for H-TiO₂ to 218.21 m²/g for GQDs-3.0/H-TiO₂ after decorating GQDs.

As revealed by SEM image (Fig. 3A), the obtained GQDs-3.0/H-TiO₂ composite completely retained the original hollow shape from H-TiO₂ and exhibited a rough surface. As can be seen in Fig. 3B, it is difficult to differentiate very small size GQDs loaded on H-TiO₂ by TEM. Inset in Fig. 3B is an electron diffraction photograph of H-TiO₂, and the regular diffraction fringes shows that the H-TiO₂ has been completely crystallized. As shown in Fig. 3C, the wall thickness of H-TiO₂ is about 25 nm, and the white translucent area appearing in the shell is interpreted as the characteristic of the mesopores. Figure 3D shows the HRTEM image of GQDs-3.0/H-TiO₂ composite, and GQDs are evenly distributed on the surface and pores of H-TiO₂. Figure 3E, F shows the typical TEM and HRTEM images of GQDs. They are spherical nanoparticles with an average particle size of 5 ± 0.5 nm; HRTEM image shows the high crystallinity of the GQDs, and the lattice spacing of 0.24 nm corresponds to the (1120) lattice spacing of graphene [51, 52]. The rich

oxygen-containing functional groups of GQDs and –OH on TiO₂ promoted the formation of the stable interfacial interactions. These results indicated that the closed interface between GQDs and H-TiO₂ formed a heterojunction which was favorable for the rapid transfer of photoinduced charges and collected electrons and holes on different sides of heterojunction.

The element status of GQDs and GQDs/H-TiO₂ was investigated by XPS. As shown in Fig. S2, C, O, and N elements are detected by XPS, revealing that the N-doping of GQDs. The high-resolution spectra of C 1s (Fig. S2B) include five prominent peaks which appear at 284.7, 285.2, 285.4, 286.1, and 289.1 eV, corresponding to C=C, C–C, C–N, C–O, and C=O, respectively [53]. And in Fig. S2C, there are three peaks at 531.5, 532.5, and 533.9 eV, which can be attributed to the –OH, C=O, and C–O–C bands, respectively. The N 1s spectra of GQDs (Fig. S2D) represent pyridine N at 399.82 eV, pyrrolic N at 400.6 eV, graphite N at 401.3 eV, and oxidized N (N+) at 402.1 eV [54]. Figure 4A shows the XPS spectrum of GQDs-3.0/H-TiO₂, as in the FTIR spectrum; the results show that GQDs and H-TiO₂

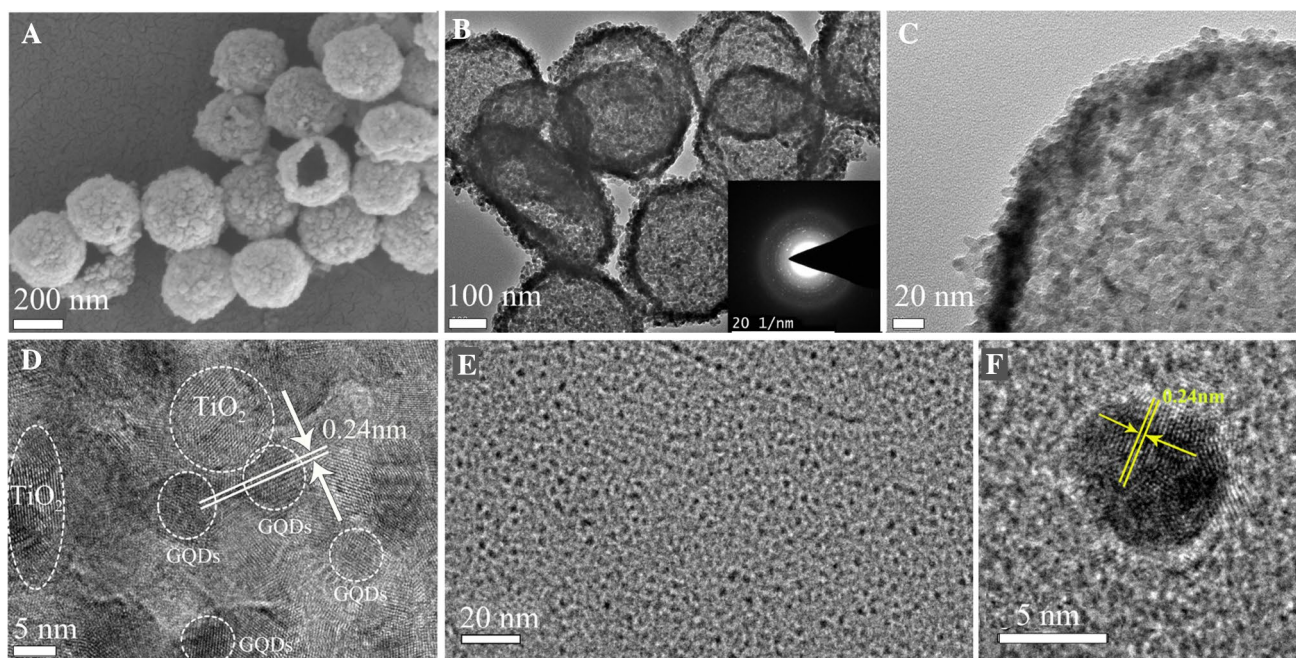


Fig. 3 **A** SEM image of GQDs-3.0/H-TiO₂. **B** and **C** TEM image of GQDs-3.0/H-TiO₂, inside illustration is electro diffraction diagram of bare H-TiO₂. **D** HRTEM images of GQDs-3.0/H-TiO₂. **E** and **F** TEM and HRTEM images of GQDs

are successfully compounded. High-resolution C 1s spectra (Fig. 4B) can be deconvoluted into four different bands which correspond to C=C at 284.75 eV, C–C at 285.2 eV, C–N/C–O at 285.9 eV, C=O at 289.05 eV. Furthermore, the high resolution of O 1s (Fig. 4C) can be deconvoluted into three bands which correspond to Ti–O at 529.1 eV, C–OH at 530.6 eV, and C=O at 531.9 eV. The high-resolution Ti 2p spectra (Fig. 4D) can be deconvoluted into two main bands which correspond to Ti 2p_{1/2} at 464.02 eV, Ti 2p_{3/2} at 458.35 eV [55].

3.2 UV-vis and photoluminescence (PL) performance analysis

To elucidate the optical properties of GQDs, H-TiO₂, GQDs-1.5/H-TiO₂, GQDs-3.0/H-TiO₂, and GQDs-4.5/H-TiO₂ composites, the UV-vis absorption and PL spectroscopy of the samples were measured. As shown in Fig. S3., GQDs exhibit obvious absorption in the whole ultraviolet region and partially in visible region. The broad and prominent absorption between 200 and 250 nm can probably be attributed to the π - π^* electron transition of graphene sp² domains. The absorption between 250 and 500 nm is mainly attributed to n - π^* electron transition, closely related to the high PL properties of GQDs [21, 56]. With incorporation of GQDs in composites, the absorption of GQDs/H-TiO₂ prolonged from 400 to 650 nm, indicating that the efficiency of visible light utilization is enhanced. The broadening of the effective absorption of GQDs/H-TiO₂ in visible light region is

mainly related to the strong interfacial interaction between GQDs and H-TiO₂, and sample with the highest absorbance intensity is GQDs-3.0/H-TiO₂. The estimated band gap of H-TiO₂ was 3.2 eV, which was similar to the reported individual TiO₂. However, the obtained band gap of GQDs/H-TiO₂ composites was significantly reduced to 2.8 eV after decorating GQDs (see Fig. 5A1). The efficiency of electron transfer was also investigated by PL. As shown in Figs. S4 and 5B, both GQDs and H-TiO₂ exhibit strong PL emission due to the high recombination ratio of their photoinduced electron-hole pairs. However, PL emission intensity evidently decreased after decorating GQDs and the composite of GQDs-3.0/H-TiO₂ has almost no PL emission. These results demonstrated that GQDs effectively suppressed the recombination of electron-hole pairs, and also act as a photo sensitizer to prolong the lifetime of photogenerated electrons and holes, which is in accord with the previous reports [31].

3.3 Photoelectrochemical characterization of GQDs/H-TiO₂ composites

Figure 6A shows the current density of products in the range of -0.4 to 0.9 V under visible light irradiation. With the increase of bias voltage, all of the photocurrent density values of GQDs/H-TiO₂ are higher than pure H-TiO₂ at a same bias voltage. It is confirmed that photoinduced electron accumulation occurs at GQDs and then the current density is significantly increased. Electrochemical impedance spectroscopy (EIS, Nyquist plots) measurements were

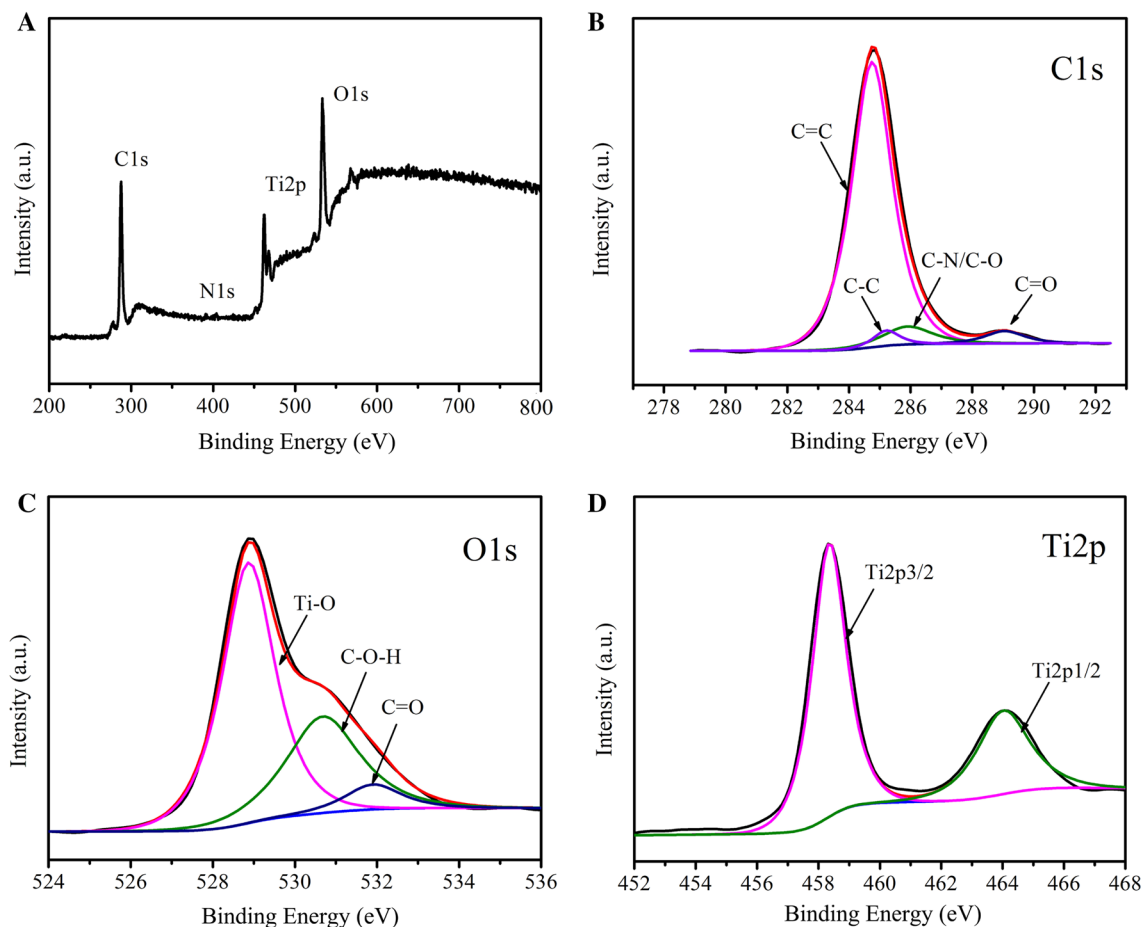


Fig. 4 A XPS spectra of GQDs-3.0/H-TiO₂. **B** C 1s, **C** O 1s, and **D** Ti 2p XPS spectrum of GQDs-3.0/H-TiO₂

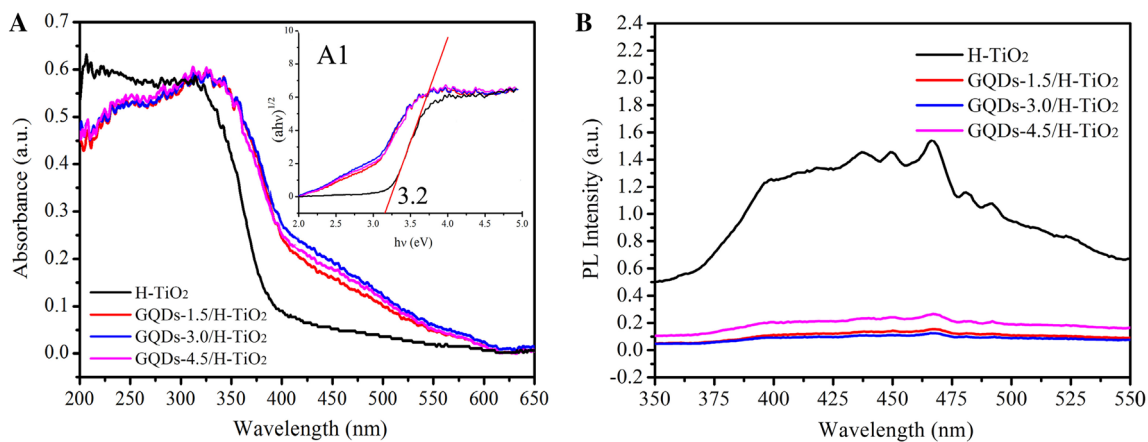


Fig. 5 A UV-vis absorption spectra of H-TiO₂, GQDs-1.5/H-TiO₂, GQDs-3.0/H-TiO₂, and GQDs-4.5/H-TiO₂. **A1** The value of the forbidden band obtained by $(ah\nu)^{1/2}$ on the slope of the photon energy.

B PL spectra of pure H-TiO₂, GQDs-1.5/H-TiO₂, GQDs-3.0/H-TiO₂, and GQDs-4.5/H-TiO₂ at 320nm excitation wavelength

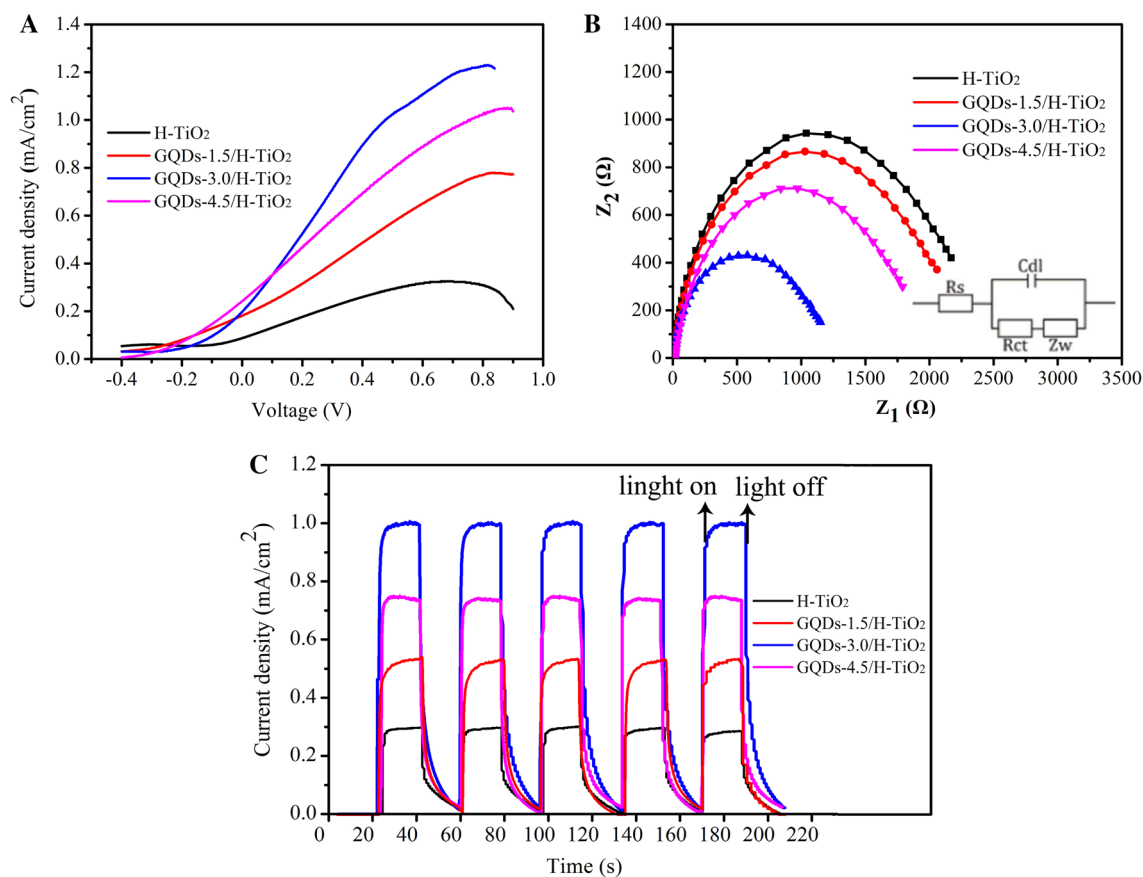


Fig. 6 **A** J - V curves and **B** EIS curves of composite materials bare H-TiO₂, GQDs-1.5/H-TiO₂, GQDs-3.0/H-TiO₂, and GQDs-4.5/H-TiO₂. **C** Transient photocurrent response spectra of H-TiO₂, GQDs-1.5/H-TiO₂, GQDs-3.0/H-TiO₂, and GQDs-4.5/H-TiO₂

carried out to research the charge transfer resistance of samples in Fig. 6B. The semi-circle of the H-TiO₂ is larger than GQDs/H-TiO₂ composites under visible light irradiation indicating a higher charge transfer resistance. The values of resistance for H-TiO₂, GQDs-1.5/H-TiO₂, GQDs-3.0/H-TiO₂, and GQDs-4.5/H-TiO₂ are 2177.5, 2070.7, 1153.5, and 1784.7 Ω , respectively. GQDs-3.0/H-TiO₂ exhibits the lowest charge transfer resistance, as we know that the lower charge transfer resistance is in favor of a higher photocurrent production [57], which is consistent with the J - V curves we described above. Thus, GQDs-3.0/H-TiO₂ has high photoelectric activity due to efficient electron-hole separation rate and fast interfacial charge transfer.

The transient photocurrent response of H-TiO₂ and GQDs/H-TiO₂ composites under repeated on and off switching is shown in Fig. 6C. Photocurrent densities of H-TiO₂, GQDs-1.5/H-TiO₂, GQDs-3.0/H-TiO₂, and GQDs-4.5/H-TiO₂ were 290, 565, 1020, 789 $\mu\text{A}/\text{cm}^2$, respectively. For the pure H-TiO₂, obviously, the photocurrent response is lower than GQDs/H-TiO₂ but higher than pure GQDs (Fig. S5). Photocurrent response of GQDs-3.0/H-TiO₂ is 3.5 times higher than that of H-TiO₂, indicating that GQDs greatly

improve the surface charge separation and transmission efficiency of materials and the optimal GQDs content is 3.0 wt% [58]. The plausible mechanism of the enhanced photoelectrochemical activity of GQDs/H-TiO₂ could be explained: the loading of GQDs optimizes the performance defects of H-TiO₂ and prolong the lifetime of photoelectrons and holes. However, the effective connection of photoexcited electrons and holes is weakened when the loading of GQDs on the surface of H-TiO₂ is excessive. Simultaneously, increased recombination rate of electron and hole pair also leads to a lower photocurrent density [50].

3.4 Photocatalytic degradation activity of GQDs/H-TiO₂ photocatalysts

Considering the excellent photoelectrochemical activity of GQDs/H-TiO₂ composites, photocatalytic degradation tests of RhB were performed to identify the photocatalytic activity under visible light irradiation ($\lambda \geq 400$ nm). As shown in Fig. 7A, different photocatalysts were added to the RhB solution and stirred 1 h to reach adsorption equilibrium in the dark. The result shows that the adsorption rate of both H-TiO₂ and

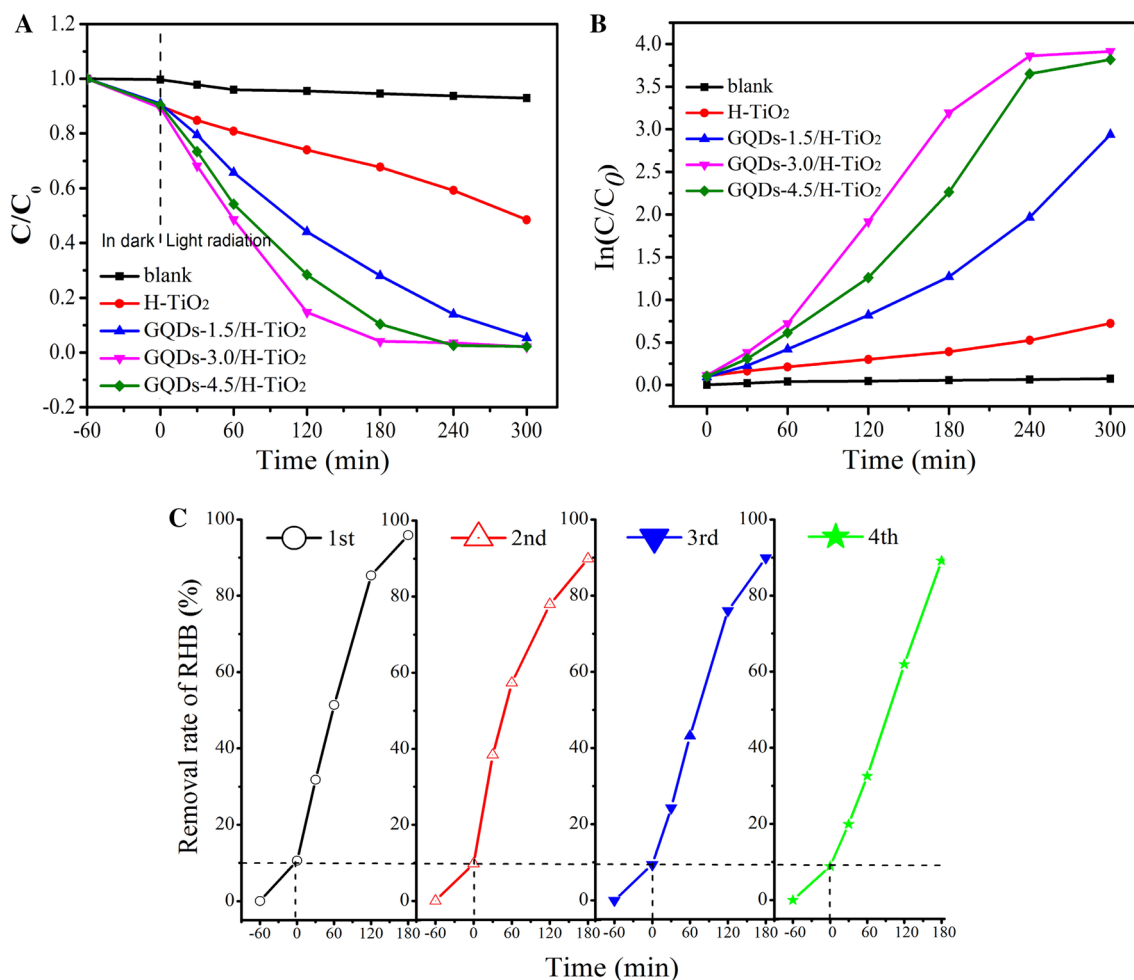


Fig. 7 **A** Photocatalytic degradation of RhB and **B** kinetic curves for H-TiO₂ and GQDs/H-TiO₂ composites. **C** Recycling test for the removal of RhB by GQDs-3.0/H-TiO₂ under visible light illumination

GQDs/H-TiO₂ composites was up to 9.0%. H-TiO₂ with hollow structure and abundant shell pores provides a large number of adsorption sites for RhB to maximally adsorb around H-TiO₂. However, the adsorption capacity of GQDs/H-TiO₂ composites did not change with increase in the content of GQDs and the test results indicated that all of GQDs/H-TiO₂ composites have the same adsorption value. GQDs with very small size have little effect on the microstructure and specific surface area of H-TiO₂, which was in conformity with the above BET tests. Photocatalytic degradation experiment was started by turning on the Xe lamp. For comparison, blank experiments were tested and almost no degradation was observed. After degradation for 180 min of RhB, reaction solution containing different catalysts was degraded and GQDs/H-TiO₂ solution was completely discolor. The 96.9% of RhB was degraded for GQDs-3.0/H-TiO₂ which is higher than H-TiO₂ (33.3%) and other GQDs/H-TiO₂ catalysts. As seen in Fig. 7B, the kinetic curves revealed that all of GQDs/H-TiO₂ shown higher photocatalytic degradation activity than pure H-TiO₂

and GQDs-3.0/H-TiO₂ with the highest activity acting as an excellent photocatalysts [57].

To further investigate photocatalytic degradation stability of the GQDs-3.0/H-TiO₂, four photocatalytic test results were recorded under the same conditions (Fig. 7C). The RhB removal rate of the GQDs-3.0/H-TiO₂ composite was maintained at 89.3% after repeated using of four times indicating that the catalyst prepared by us has outstanding stability. These mainly ascribed to the excellent electron transport properties between H-TiO₂ microsphere and GQDs due to the stable interfacial contact. Such high photocatalytic degradation stability demonstrates that the GQDs-3.0/H-TiO₂ is a promising catalyst in photocatalysis.

3.5 Photocatalytic mechanism of GQDs/H-TiO₂ photocatalysts

On the basis of the above discussions and previous literatures [25, 38, 55], a feasible photocatalytic reaction mechanism

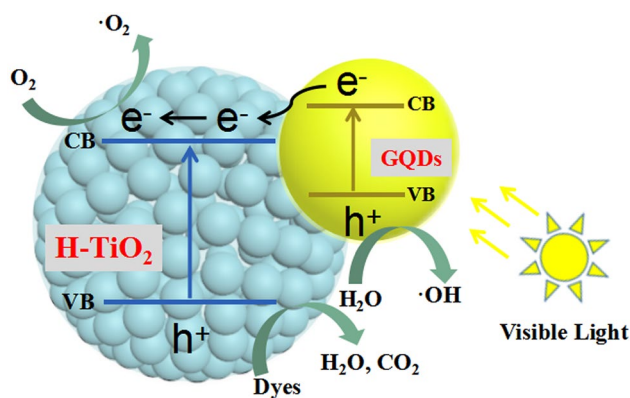


Fig. 8 Simplified mechanism for the enhanced photocatalytic activity of GQDs/H-TiO₂

for GQDs/H-TiO₂ is illustrated in Fig. 8. Typically, decorating of H-TiO₂ with GQDs could prolong the range of light absorption to be visible. The electrons of GQDs excited from valence band (VB) to conduction band (CB) under the irradiation of visible light, and then the excited electrons on the CB would transfer to the CB of H-TiO₂. GQDs can serve as an electron repository to provide electrons to H-TiO₂ so that electrons/hole (e^-/h^+) pairs can be effectively separated during the whole process. Electrons and hole can convert absorbed O₂ and H₂O into active oxygen ($\cdot O_2^-$) and hydroxyl ($\cdot OH$) radicals which both have strong oxidizability to degrade RhB molecules into CO₂, H₂O, and other intermediates. Thus, the electron separation process promotes the formation of $\cdot O_2^-$ and $\cdot OH$ radicals and explains why GQDs/H-TiO₂ has enhanced photocatalytic activity.

It is worth mentioning that GQDs play a critical role in the photocatalytic system. Initially, GQDs can be used as electron repository and transporter to accept and transfer photoelectrons. At the same time, GQDs could inhibit the rapid recombination of e^-/h^+ pairs and enhance photocatalytic activity of GQDs/H-TiO₂. In addition, the higher specific surface area of our GQDs/H-TiO₂ microspheres can provide abundant exposed active sites for the photochemical reactions. More importantly, GQDs can be applied as a novel photosensitizer to integrate into other practical applications of photocatalytic and photoelectric conversion devices.

4 Conclusions

In conclusion, we successfully synthesized the GQD decorated with H-TiO₂ nanospheres through a simple hydrothermal method. The incorporation of GQDs has a slight effect on morphology and microstructure of H-TiO₂ as confirmed by SEM, TEM, XRD, and BET analysis. The obtained GQDs/H-TiO₂ composites possess higher photoelectric

activity under visible light irradiation owing to the uniform quantum size and excellent optoelectronic performance of GQDs. The PL and photoelectrochemical characterizations indicated that GQDs can serve not as an electron repository but as an electron transport bridge. Significantly, the photocurrent response of GQDs-3.0/H-TiO₂ with the best response is 3.5 times higher than that of H-TiO₂. In addition, the photocatalytic activity of GQDs/H-TiO₂ composites was investigated and the results showed that GQDs play critical roles in enhancing the photocatalytic activity of products and GQDs-3.0/H-TiO₂ has the highest photocatalytic activity to degrade RhB. Furthermore, the mechanism for the enhanced photocatalytic activity of GQDs/H-TiO₂ was proposed. GQDs could inhibit the rapid recombination of electron–hole pairs and enlarge the visible light absorption region (650 nm) for photocatalytic transformations, and GQDs/H-TiO₂ microspheres with higher specific surface area (223.48 m²/g) can provide abundant active sites for the photochemical reactions. Moreover, this work may be extended further to prepare GQDs-modified semiconductors for the photocatalysis and photoelectrochemical conversion and also provide further insights in applying GQDs to other sensor, optoelectronic, biomedical, and energy conversion-related devices.

5 Supplementary material

Additional table of orthogonal experiment, SEM images, XPS spectrum of GQDs, UV–vis absorption spectrum of GQDs, PL spectra of GQDs, Transient photocurrent response spectra of the GQDs, etc.

Acknowledgements This research was supported by the Research Center of Gansu Military and Civilian Integration Advanced Structural Materials, the National Natural Science Foundation of China (No. 51262027), the Science and Technology Project Gansu Province (17JR5RA082), and the State Key Laboratory of Solidification Processing in NWPU (No. SKLSP201754).

References

1. L. Ponomarenko, F. Schedin, M. Katsnelson, R. Yang, E. Hill, K. Novoselov, A. Geim, *Science* **320**, 356–358 (2008)
2. J. Shen, Y. Zhu, X. Yang, C. Li, *Chem. Commun.* **48**, 3686–3699 (2012)
3. X. Fang, J. Ding, N. Yuan, P. Sun, M. Lv, G. Ding, C. Zhu, *Phys. Chem. Chem. Phys.* **19**, 6057–6063 (2017)
4. M.L. Tsai, W.C. Tu, L. Tang, T.C. Chiao, W.R. Wei, S.P. Lau, L.J. Chen, J.H. He, *Nano Lett.* **16**, 309–313 (2016)
5. F. Bonaccorso, L. Colombo, G.H. Yu, M. Stoller, V. Tozzini, A.C. Ferrari, R.S. Ruoff, V. Pellegrini, *Science* **347**, 1246501 (2015)
6. H. Sun, L.I. Wu, W. Wei, X. Qu, *Mater. Today* **16**, 433–442 (2013)
7. Y. Zhou, Z.-B. Qu, Y. Zeng, T. Zhou, G. Shi, *Biosens. Bioelectron.* **52**, 317–323 (2014)

8. X.T. Zheng, A. Ananthanarayanan, K.Q. Luo, P. Chen, *Small* **11**, 1620–1636 (2015)
9. T. Chen, H. Yu, N. Yang, M.D. Wang, C. Ding, J. Fu, *J. Mater. Chem. B* **2**, 4979–4982 (2014)
10. S. Pitchaimuthu, H.C. Isaac, P. Hun, T. Song, H.N. Seung, G. Sixto, M.S. Ivan, F.S. Francisco, B. Juan, T. Chiaki, P. Ungyu, S.K. Yong, F. Akira, H.H. Tae, *Electrochim. Acta* **187**, 249–255 (2016)
11. Z. Yang, Z. Yao, G.F. Li, G.Y. Fang, H.G. Nie, Z. Liu, X.M. Zhou, X.A. Chen, S.M. Huang, *ACS Nano* **6**, 205–211 (2012)
12. L. Wang, Y. Wang, T. Xu, H. Liao, C. Yao, Y. Liu, Z. Li, Z. Chen, D. Pan, L. Sun, M. Wu, *Nat. Commun.* **5**, 5357 (2014)
13. H. Ding, S.B. Yu, J.S. Wei, H.M. Xiong, *ACS Nano* **10**, 484–491 (2016)
14. D. Qu, M. Zheng, P. Du, Y. Zhou, L. Zhang, D. Li, H. Tan, Z. Zhao, Z. Xie, Z. Sun, *Nanoscale* **5**, 12272–12277 (2013)
15. Y. Han, D. Tang, Y. Yang, C. Li, W. Kong, H. Huang, Y. Liu, Z. Kang, *Nanoscale* **7**, 5955–5962 (2015)
16. Y. Li, Y. Hu, Y. Zhao, G.Q. Shi, L.E. Deng, Y.B. Hou, L.T. Qu, *Adv. Mater.* **23**, 776–780 (2011)
17. S.J. Zhu, J.H. Zhang, S.J. Tang, C.Y. Qiao, L. Wang, H.Y. Wang, X. Liu, B. Li, Y.F. Li, W.L. Yu, X.F. Wang, H.C. Sun, B. Yang, *Adv. Funct. Mater.* **22**, 4732–4740 (2012)
18. P. Elvati, E. Baumeister, A. Violi, *RSC Adv.* **7**, 17704–17710 (2017)
19. Y.-P. Sun, B. Zhou, Y. Lin, W. Wang, K.S. Fernando, P. Pathak, M.J. Meziani, B.A. Harruff, X. Wang, H. Wang, *J. Am. Chem. Soc.* **128**, 7756–7757 (2006)
20. S. Zhu, J. Zhang, C. Qiao, S. Tang, Y. Li, W. Yuan, B. Li, L. Tian, F. Liu, R. Hu, *Chem. Commun.* **47**, 6858–6860 (2011)
21. L. Li, G. Wu, G. Yang, J. Peng, J. Zhao, J.J. Zhu, *Nanoscale* **5**, 4015–4039 (2013)
22. Y. Li, Y. Zhao, H. Cheng, Y. Hu, G. Shi, L. Dai, L. Qu, *J. Am. Chem. Soc.* **134**, 15–18 (2012)
23. H. Xie, C.Y. Hou, H. Wang, Q. Zhang, Y. Li, *Nanoscale Res. Lett.* **12**, 400 (2017)
24. S. Bian, C. Zhou, P. Li, J. Liu, X. Dong, F. Xi, *ChemCatChem* **9**, 3349–3357 (2017)
25. X.J. Yu, J.J. Liu, Y.C. Yu, S.L. Zuo, B.S. Li, *Carbon* **68**, 718–724 (2014)
26. M. Ramezani, S.M. Hosseinpour-Mashkani, *J. Electron. Mater.* **46**, 1371–1377 (2017)
27. S.M. Hosseinpour-Mashkani, A. Sobhani-Nasab, *J. Mater. Sci. Mater. Electron.* **28**, 4345–4350 (2017)
28. G. Liu, H.G. Yang, X.W. Wang, L. Cheng, J. Pan, G.Q. Lu, H.M. Cheng, *J. Am. Chem. Soc.* **131**, 12868–12869 (2009)
29. S. Sadhu, P. Poddar, *J. Phys. Chem. C* **118**, 19363–19373 (2014)
30. L. Wan, M.C. Long, D.Y. Zhou, L.Y. Zhang, W.M. Cai, *Nano-Micro Lett.* **4**, 90–97 (2012)
31. Z. Xu, M. Yin, J. Sun, G. Ding, L. Lu, P. Chang, X. Chen, D. Li, *Nanotechnology* **27**, 115401 (2016)
32. Z. Bai, Y. Zhang, *J. Alloys Compd.* **698**, 133–140 (2017)
33. N. Buatong, I.-M. Tang, P.-O. Weeraphat, *Nanoscale Res. Lett.* **12**, 170 (2017)
34. K. Woan, G. Pyrgiotakis, W. Sigmund, *Adv. Mater.* **21**, 2233–2239 (2009)
35. Y. Zheng, Y. Jiao, L. Ge, M. Jaroniec, S.Z. Qiao, *Angew. Chem.* **52**, 3110–3116 (2013)
36. Y. Dai, Y. Sun, J. Yao, D. Ling, Y. Wang, H. Long, X. Wang, B. Lin, T.H. Zeng, Y. Sun, *J. Mater. Chem. A* **2**, 1060–1067 (2014)
37. K.A.S. Fernando, S. Sahu, Y. Liu, W.K. Lewis, E.A. Gulians, A. Jafariyan, P. Wang, C.E. Bunker, Y.-P. Sun, *ACS Appl. Mater. Interfaces* **7**, 8363–8376 (2015)
38. A. Qu, H. Xie, X. Xu, Y. Zhang, S. Wen, Y. Cui, *Appl. Surf. Sci.* **375**, 230–241 (2016)
39. R. Ye, C. Xiang, J. Lin, Z. Peng, K. Huang, Z. Yan, N.P. Cook, E.L. Samuel, C.C. Hwang, G. Ruan, G. Ceriotti, A.R. Raji, A.A. Marti, J.M. Tour, *Nat. Commun.* **4**, 2943 (2013)
40. J. Peng, W. Gao, B.K. Gupta, Z. Liu, R. Romero-Aburto, L. Ge, L. Song, L.B. Alemany, X. Zhan, G. Gao, S.A. Vithayathil, B.A. Kaiparettu, A.A. Marti, T. Hayashi, J.J. Zhu, P.M. Ajayan, *Nano Lett.* **12**, 844–849 (2012)
41. D.C. Marcano, D.V. Kosynkin, J.M. Berlin, A. Sinitskii, Z.Z. Sun, A. Slesarev, L.B. Alemany, W. Lu, J.M. Tour, *ACS Nano* **4**, 4806–4814 (2010)
42. H. Liu, H.L. Li, Z.L. Ding, A.P. Fu, H.Y. Wang, P.Z. Guo, J.Q. Yu, C.G. Wang, X.S. Zhao, *J. Clust. Sci.* **23**, 273–285 (2012)
43. Y. Wan, S.H. Yu, *J. Phys. Chem. C* **112**, 3641–3647 (2008)
44. B. Friedel, S. Greulich-Weber, *Small* **2**, 859–863 (2006)
45. A. Bayat, E. Saievar-Iranizad, *J. Energy Chem.* **27**, 306–310 (2018)
46. M. Fu, F. Ehrat, Y. Wang, K.Z. Milowska, C. Reckmeier, A.L. Rogach, J.K. Stolarczyk, A.S. Urban, J. Feldmann, *Nano Lett.* **15**, 6030–6035 (2015)
47. S. Wang, I.S. Cole, D. Zhao, Q. Li, *Nanoscale* **8**, 7449–7458 (2016)
48. X. Hao, Z. Jin, J. Xu, S. Min, G. Lu, *Superlattice Microstruct.* **94**, 237–244 (2016)
49. S.D. Perera, R.G. Mariano, K. Vu, N. Nour, O. Seitz, Y. Chabal, K.J. Balkus, *ACS Catal.* **2**, 949–956 (2012)
50. Y. Yan, Q. Liu, X. Du, J. Qian, H. Mao, K. Wang, *Anal. Chim. Acta* **853**, 258–264 (2015)
51. C. Zhu, S. Yang, G. Wang, R. Mo, P. He, J. Sun, Z. Di, Z. Kang, N. Yuan, J. Ding, G. Ding, X. Xie, *J. Mater. Chem. B* **3**, 6871–6876 (2015)
52. X. Tan, Y. Li, X. Li, S. Zhou, L. Fan, S. Yang, *Chem. Commun.* **51**, 2544–2546 (2015)
53. S.H. Jin, D.H. Kim, G.H. Jun, S.H. Hong, S. Jeon, *ACS Nano* **7**, 1239–1245 (2013)
54. Z. Xue, G. Hui, X. Li, *Dyes Pigments* **156**, 379–385 (2018)
55. S.X. Min, J. Hou, Y. Lei, X. Ma, G.X. Lu, *Appl. Surf. Sci.* **396**, 1375–1382 (2017)
56. J. Sun, S. Yang, Z. Wang, H. Shen, T. Xu, L. Sun, H. Li, W. Chen, X. Jiang, G. Ding, Z. Kang, X. Xie, M. Jiang, *Part. Part. Syst. Charact.* **32**, 434–440 (2015)
57. N. Singh, K. Mondal, M. Misra, A.S. Iitk, *RSC Adv.* **6**, 48109–48119 (2016)
58. H. Safardousthojaghan, M. Salavatinasari, *J. Clean. Prod.* **148**, 31–36 (2017)

Publisher's Note Springer Nature remains neutral with regard to jurisdictional claims in published maps and institutional affiliations.